

Article

Mineralogical and Geochemical Characterization of Asbestiform Todorokite, Birnessite, and Ranciéite, and Their host Mn-Rich Deposits from Serra D’Aiello (Southern Italy)

Andrea Bloise ¹, Domenico Miriello ¹, Rosanna De Rosa ^{1,*}, Giovanni Vespasiano ^{1,2,*},
Iliaria Fuoco ¹, Raffaella De Luca ¹, Eugenio Barrese ¹ and Carmine Apollaro ¹

¹ Department of Biology, Ecology and Earth Sciences, University of Calabria, Via Pietro Bucci, 87036 Rende, CS, Italy; andrea.bloise@unical.it (A.B.); domenico.miriello@unical.it (D.M.); ilaria.fuoco@unical.it (I.F.); raffaella.deluca@unical.it (R.D.L.); e.barrese@unical.it (E.B.); apollaro@unical.it (C.A.)

² E3 (Environment, Earth, Engineering) soc.coop. (University of Calabria), 87036 Rende, CS, Italy

* Correspondence: derosa@unical.it (R.D.R.); giovanni.vespasiano@unical.it (G.V.);
Tel.: +39-0984-493690 (R.D.R.); +39-0984-493580 (G.V.)

Received: 8 December 2019; Accepted: 26 January 2020; Published: 28 January 2020



Abstract: Manganese ores, especially the oxyhydroxides in their different forms, are the dominant Mn-bearing minerals that occur in marine and terrestrial environments, where they are typically found as poorly crystalline and intermixed phases. Mn oxyhydroxides have a huge range of industrial applications and are able to exert a strong control on the mobility of trace metals. This paper reports the results of a detailed study on the Mn oxyhydroxides occurring in the manganiferous deposit outcropping in the Messinian sediments from Serra D’Aiello (Southern Italy). Nine Mn samples were characterized in detail using X-ray powder diffraction (XRPD), differential scanning calorimetry (DSC), thermogravimetry (TG), transmission electron microscopy combined with energy dispersive spectrometry (TEM/EDS), and X-ray fluorescence (XRF). The results indicated that the Mn deposit included the oxyhydroxide mineral species birnessite, todorokite, and ranciéite. The size, morphology, and chemical composition of Mn oxyhydroxide samples were investigated in order to define their impact on the environment and human health. Todorokite displayed asbestiform shapes and could disperse fibers of breathable size in the air. Furthermore, since in-depth characterization of minerals within Mn deposits may be the first step toward understanding the genetic processes of manganese deposits, hypotheses about the genesis of the Mn oxyhydroxide deposits were discussed.

Keywords: Mn oxyhydroxides; todorokite; ranciéite; birnessite; asbestiform; human health

1. Introduction

Manganese (Mn) deposits occur in both marine and terrestrial environments as a mix of Mn oxyhydroxides. It is within the marine environment, independent of deep and oxygenated conditions, that the most important Mn deposits are formed. Considering their formation and composition, Mn oxyhydroxide deposits can be classified as hydrogenous, diagenetic, and/or hydrothermal [1]. In both hydrothermal and diagenetic occurrences, Mn oxyhydroxides may exhibit different crystal habits (lamellar, needle-like, fibrous, and asbestiform) [2–8].

Generally, hydrogenous Mn deposits are slowly precipitated from seawater, diagenetic Mn oxyhydroxides are formed by the diagenesis of Mn-rich protolith, and hydrothermal Mn oxyhydroxides are directly precipitated from geothermal solutions around hot springs [9].

Mn oxyhydroxide minerals are a potential economic resource [10]. In particular, todorokite $[(\text{Na,Ca,K,Ba,Sr})_{1-x}(\text{Mn,Mg,Al})_6\text{O}_{12}\cdot 3\text{--}4\text{H}_2\text{O}]$ has many potential industrial applications, such as sorbents, sensors, heterogeneous catalysts, and rechargeable batteries [11]. Regarding birnessite $[(\text{Na,Ca})_{0.5}(\text{Mn})_2\text{O}_4\cdot 1.5\text{H}_2\text{O}]$, it has been used in previous works as a catalyst in soot combustion processes and in methylene blue degradation, showing appreciable catalytic activity compared to traditional catalysts [12]. Ranciéite $[(\text{Ca,Mn}^{2+})\text{Mn}^{4+}4\text{O}_9\cdot 3\text{H}_2\text{O}]$ is known to be an efficient adsorbent of toxic metals, such as plutonium [13]. Despite their economic use, Mn oxyhydroxide deposits could pose an environment problem, as they could contaminate the air, soils, sediments, surface water, and groundwater [14]. Some studies have reported associations between Mn exposure and adverse health effects [15–18], while other studies suggest that Mn-rich water can be neurotoxic for both adults and for children [19–22].

Another aspect to consider is that some Mn oxyhydroxides, such as todorokite and manjiroite, can crystallize, exhibiting an asbestiform morphology [5–7]. It is worth mentioning that asbestiform minerals (e.g., erionite, ferrierite, and fluor-edenite) are sometimes more dangerous than the six regulated asbestos fibers (chrysotile, amosite, crocidolite, anthophyllite, tremolite, and actinolite) [23,24]. Indeed, non-regulated fibers, such as erionite, ferrierite, and fluor-edenite, are considered to be positive carcinogen minerals [25–27]. As such, the US National Institute for Occupational Safety and Health (NIOSH) [28] has recently proposed to extend the definition of asbestos to all elongated mineral particles (EMPs) [29].

The issue is even more complicated as minerals with fibrous and lamellar habits are often found together within the same deposits and the same rocks [29–32], and these minerals must be discriminated correctly from a morphological point of view. In this regard, NIOSH highlights the difficulty in ascertaining the source of exposure in the case of mixed exposures (i.e., asbestos, asbestiform minerals, lamellar minerals) for some mining operations. A large amount of Mn oxyhydroxides with fibrous-asbestiform habits are observed in deposits that can eventually be mined and used for industrial applications [5,7]. Disturbance (i.e., erosion, excavation, road construction, agricultural activities) of these outcrops can generate airborne fibers with a similar size to asbestos fibers, thus increasing the hazard to people who live near these deposits.

As a matter of fact, only sporadic studies were devoted to Mn deposit outcroppings in the Messinian sediments from the Serra D’Aiello area [33–35]. In this contest, we have collected and studied in detail nine Mn-rich samples occurring in the manganiferous deposit outcropping in the Messinian sediments from Serra D’Aiello (Southern Italy) by combining X-ray powder diffraction (XRPD), differential scanning calorimetry (DSC), thermogravimetry (TG), transmission electron microscopy combined with energy dispersive spectrometry (TEM/EDS), and X-ray fluorescence (XRF) in order to: (i) inspect their possible mineralogical hazardous nature, (ii) evaluate their potential for releasing contaminant elements into soils or waters, and (iii) identify their environmental formation.

2. Geological Setting

The studied Mn deposit outcrop in the Serra D’Aiello area in the southern boundary of the Amantea Basin sedimentary sequence in Southern Italy is shown in Figure 1.

The basin is characterized by two main sedimentation cycles: a Tortonian-Messinian cycle (TMC) and a Messinian-Lower Pliocene cycle (MLPC), which are divided by a compressive tectonic intramessinian event [37–39]. The TMC formed during a transgressive phase that progressively affected the entire basin and consists of conglomerates and sandy-silty terrains, indicating a transition from a continental (coastal alluvial plain) to a marine environment [40], as recognized using the following terrains in the TMC: (i) red conglomerates, (ii) sandstone, (iii) cinerites, (iv) fossiliferous conglomerates, (v) arenaceous calcarenites, (vi) clays, and (vii) diatomites at the top of the sequence (deep sea conditions). The Mn deposit outcrops in correspondence to the cyclical arenaceous-clayey alternations, whose total thickness is just under 30 meters, overlies the gray fossiliferous clays (Figure 2) and is laterally observed (in the outcrop) for about 150 m, providing a detailed lithostratigraphic

description of the Mn outcrop and highlighting the presence of mineralization made up by autogenous minerals, such as Mn hydrated oxides.

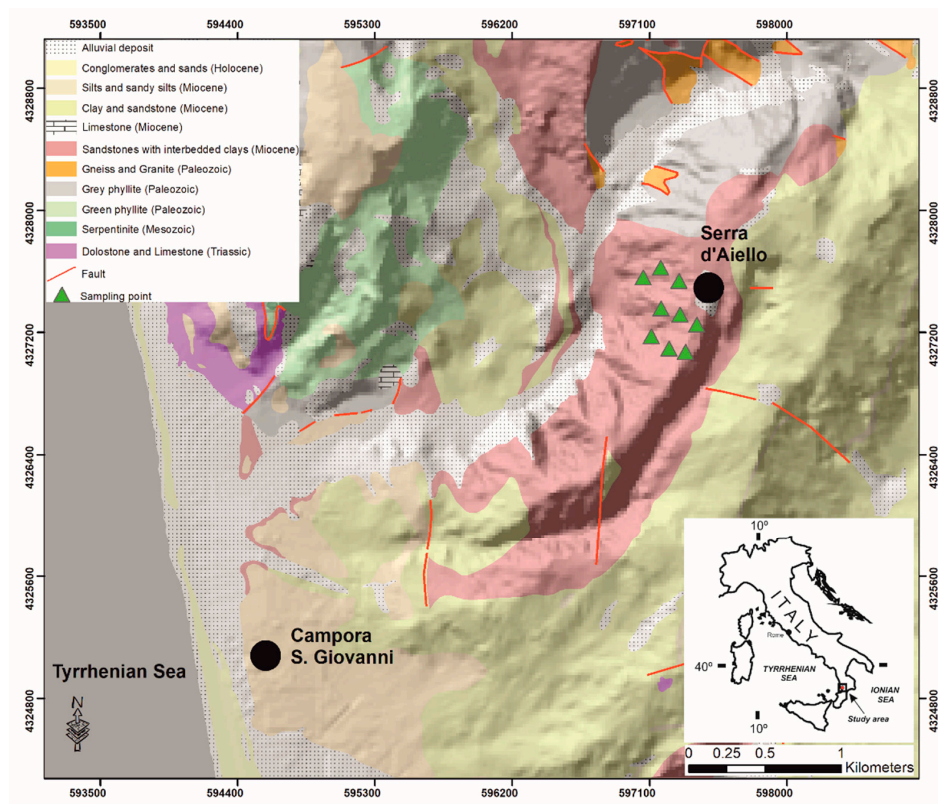


Figure 1. Simplified geological map of the investigated area (modified after CASMEZ [36]).



Figure 2. Distant view of the alternation of gray silty layers and manganese (black) layers from Serra D'Aiello (Southern Italy).

The first cycle is interrupted by the Messinian tectonic phase, which has a compressive character in the Amantea basin, as evidenced by the shortening of the original basin. After this tectonic phase, sedimentation resumed (cycle II—MLPC) and the terrains were deposited in discordance over the previous cycle, and in some places, directly on the crystalline-metamorphic basement. The recognized succession is constituted by: (i) polygenic conglomerates; (ii) evaporitic limestones and limestones; and (iii) sandstones, clay, and silty clay [40].

3. Materials and Methods

Nine Mn-rich samples were collected and studied using different analytical techniques to obtain a detailed mineralogical and geochemical characterization [41,42]. The collected samples were all black in color and showed a massive appearance. The samples were preliminarily inspected under reflected light using a Zeiss Axioskop 40 microscope (Zeiss, Jena, Germany) in order to choose representative single nodules (i.e., free from alterations) to be studied using X-ray powder diffraction analysis (XRPD), differential scanning calorimetry (DSC), and thermogravimetry (TG).

The bulk geochemical composition of major (SiO_2 , TiO_2 , Al_2O_3 , Fe_2O_3 , MnO , MgO , CaO , Na_2O , K_2O , P_2O_5) and trace (Ni, Cr, V, Co, Ba, Sr, Cu, Zn, Pb) elements were obtained using X-ray fluorescence (XRF). Chemical elements were analyzed with a rhodium tube with a 40 kW intensity using a Bruker S8 Tiger (Bruker, Karlsruhe, Germany) X-ray fluorescence device (Tables 3 and 4). Chemical data were processed according to the Aitchison model in order to calculate the centered-log-ratio (clr) transformations.

XRPD patterns were obtained on a Bruker D8 Advance X-ray diffractometer (Bruker, Karlsruhe, Germany) with $\text{CuK}\alpha$ radiation, monochromated with a graphite sample monochromator at 40 kV and 40 mA. Scans were collected in the range of $3\text{--}66^\circ 2\theta$, with a step interval of $0.02^\circ 2\theta$ and step-counting time of 3 seconds. EVA software (DIFFRACplus EVA version 11.0. rev. 0) was used to identify the mineral phases in each X-ray powder pattern with experimental peaks being compared with 2005 PDF2 reference patterns. Differential scanning calorimetry (DSC) and thermogravimetry (TG) were performed in an alumina crucible under a constant nitrogen flow of $30 \text{ cm}^3 \text{ min}^{-1}$ with a Netzsch STA 449 C Jupiter (Netzsch-Gerätebau GmbH, Selb, Germany) in a $25\text{--}1000^\circ \text{C}$ temperature range and a heating rate of $10^\circ \text{C}/\text{min}$. Derivative thermogravimetry (DTG), derivative differential scanning calorimetry (DDSC) and endothermic peaks were obtained using Netzsch Proteus thermal analysis software, version 4.7.0. The instrumental precision was checked via repeated collections on a kaolinite reference sample (six collections), revealing a good reproducibility (instrumental theoretical T precision of $\pm 1.2^\circ \text{C}$) and a theoretical weight sensitivity of $0.10 \mu\text{g}$. For DSC/TG and XRPD investigations, samples were ground in an agate mortar. The size, crystallinity, structural features, and chemical composition of single particles were determined using a Jeol JEM 1400 Plus (120 kV) transmission electron microscope (TEM; Jeol, Tokyo, Japan) equipped with a double tilt holder to obtain structural data using selected area electron diffraction (SAED) and with a Jeol large-area silicon drift detector SDD-EDS (Jeol Tokyo, Japan) for microanalyses. For TEM investigations, the sample was put in isopropyl alcohol and then sonicated. Two drops of the obtained suspension were deposited on a Formvar carbon-coated copper grid. In order to describe the size (length and diameter) of the fibers, several dozen TEM micrographs were recorded and six single fibers of todorokite for each sample were measured.

4. Results and Discussion

4.1. Field Observation

Serra D'Aiello's Mn deposits were localized in correspondence with the cyclical arenaceous-clayey alternations (Figure 2). The deposits were stratified showing layers with thicknesses varying from a few mm up to 30 cm and were also oriented parallel to the direction of the silty layers (Figure 3a-d). Within the layers, the Mn oxyhydroxides were deposited in laminae or nodules of variable dimensions.

The latter were constituted by a shell of hydroxides of Mn that enclosed a core of silt (Figure 3e). Their shape was ellipsoidal with a larger diameter ranging from 2–3 cm up to 22 cm and were oriented with the largest diameter parallel to the direction of the layers.

The larger nodules contained smaller nodules and had a thin shell, whereas those that were smaller in size did not contain nodules and had a thicker shell. Within the silty layers, there were also some levels (at least three) with iron oxides (Figure 3f). These were sometimes constituted by nodules and dimensions of less than 3 cm, whereas in others, they formed laminae with a thickness of about 1 cm. Both the layers and the iron oxide nodules were oriented parallel to the direction of the silty layers. The mineralized layers had been affected by a series of faults, bringing them to different heights and constructing a stepped structure.

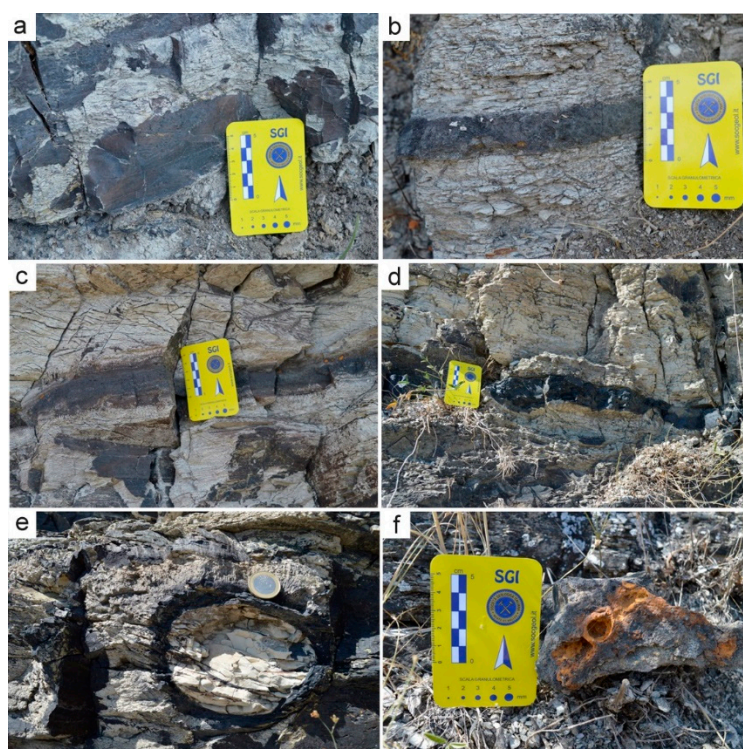


Figure 3. Typical morphology of the Mn oxyhydroxide deposits at the mesoscale, (a–d) alternation of gray silty layers and black manganese layers, (e) ellipsoidal black manganese nodule, and (f) iron oxide nodules inside the black manganese layers.

4.2. XRPD and DSC/TG Characterization

The minerals detected in the studied samples are listed in Table 1. The evaluation of the XRPD patterns showed that Mn oxyhydroxides were the main phases identified in all samples. The diffraction peaks were found to match with the standard, provided by the International Centre for Diffraction Data (ICDD) [43], of birnessite (ICDD 23-1046), todorokite (ICDD 19-83 and ICDD 21-553) and ranciéite (ICDD 22-718). Quartz, calcite, plagioclase, K-feldspar, rhodochrosite, and muscovite were also detected in varying amounts but not in all samples.

The XRPD patterns of birnessite and ranciéite generally showed broad reflections (Supplementary Materials Figure S1), suggesting that poorly crystalline phases were present in the samples. On the other hand, the XRPD pattern of todorokite was characterized by less broad peaks, indicating a moderate level of crystallinity. The mixed Mn oxyhydroxides (i.e., todorokite, birnessite, and ranciéite) were also proven using a thermal analysis collapse temperature in agreement with the literature data [44–46]. In particular, the DSC curves showed an endothermic effect at around 200 °C (Figure 4; Table 2) due to the breakdown of birnessite [44]. The DSC curve of ranciéite exhibited one endothermic effect in the

range 640–680 °C (Figure 4; Table 2) [45]. Finally, the DSC curve of todorokite showed one shoulder effect at about 460 °C (Figure 4; Table 2), which was clearly recorded on the DDSC curve, related to its structural collapse [46]. The very weak endothermic effect in the range 575–597 °C (Figure 4; Table 2) was due to the structural $\alpha \rightarrow \beta$ transition of quartz [47], while the endothermic peak at 806 °C (sample 3S) corresponded to the breakdown of muscovite in agreement with Földvári [47]. The endothermic peak at 570 °C (sample 7S) and in the range 743–798 °C (samples 3S, 4S, and 8S) on the DSC curve, which were also clearly recorded on the DTG curve (not shown), were due to the decarbonation of rhodochrosite [47] and calcite [47], respectively. The endothermic peaks on the DSC curves below 110 °C (Figure 4) were attributed to the release of water adsorbed on the samples’ surfaces.

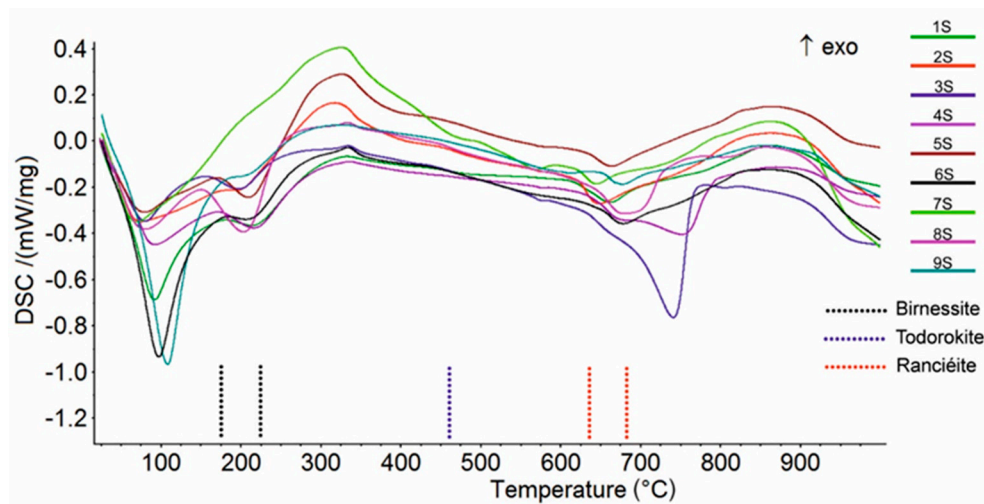


Figure 4. Comparison between DSC curves of the Mn oxyhydroxides samples.

Table 1. Location of each collected sample (geo-referenced using Universal Transverse of Mercator (UTM) coordinates system and World Geodetic System 1984 (WGS84) as ellipsoid), and their semi-quantitative mineralogical assemblage in order of decreasing abundance as detected using XRPD, DSC/TG, and TEM/EDS. Ranc = ranciéite, Birn = birnessite, Todor = todorokite, Qtz = quartz, Plag = plagioclase, Ms = muscovite, K-feld = K-feldspar, Cal = calcite, Rod = rhodochrosite.

Samples	X		Y		Phases
	UTM (WGS84)		UTM (WGS84)		
1S	597057.462	4327544.556			Ranc> Birn>Todor>K-feld
2S	597169.537	4327610.483			Ranc> Birn>Todor>Qtz>Plag>K-feld
3S	597288.205	4327528.075			Birn>Ranc>Cal>Todor>Qtz>Plag>K-feld>Ms
4S	597166.241	4327330.295			Birn>Ranc>Todor>Cal>Qtz>Plag>K-feld
5S	597301.39	4327294.035			Ranc>Birn>Todor>Qtz>Plag>K-feld
6S	597413.465	4327244.59			Ranc>Birn>Qtz
7S	597113.499	4327162.182			Todor>Ranc>Rod>Qtz
8S	597228.871	4327076.478			Birn>Ranc>Qtz>Cal>Plag
9S	597331.057	4327063.293			Ranc>Birn>Qtz

Table 2. Peak temperatures (°C) in DSC curves; w—weak, s—strong, sh—shoulder, endo—endothermic. Exothermic peaks have not been reported.

Phases	DSC (°C)								
	1S	2S	3S	4S	5S	6S	7S	8S	9S
Water/humidity	92 endo s	80 endo s	80 endo s	93 endo s	80 endo s	97 endo s	70 endo s	80 endo s	108 endo s
Birnessite	214 endo s	190 endo w	197 endo s	216 endo s	210 endo s	206 endo	-	204 endo	208 endo
Todorokite	472 sh	460 sh	423 sh	443 sh	480 sh	-	474 endo w	-	-
Quartz	-	575 endo	575 endo	576 endo	576 endo	597 endo	-	577 endo	598 endo
Rhodochrosite	-	-	-	-	-	-	570 endo	-	-
Ranciéite	661 endo s	650 endo s	670 sh	681 endo	663 endo s	677 endo s	643 endo s	678 endo	678 endo s
Calcite	-	-	743 endo s	751 endo s	-	-	-	798 endo	-
Muscovite	-	-	806 endo	-	-	-	-	-	-

4.3. TEM/EDS Characterization

The identification of mineral components and the characterization of the morphologies using scanning electron microscopy (SEM) were not undertaken due to the colloidal texture and nanometer-scale sizes of the Mn oxyhydroxides. Indeed, both secondary and backscattered electron images did not show any detailed features of the Mn oxyhydroxides. In light of this, as well as the characteristics and regarding the nanometric dimensions of the Mn oxyhydroxides layers, TEM was used due to its high magnification power.

A representative set of TEM micrographs showing the morphology of Mn oxyhydroxides observed in the various samples are given in Figures 5 and 6. In accordance with literature data [48], TEM observations of birnessite showed crumpled sheet morphologies (Figure 5a), all characterized by rather poor crystallinity (Figure 5a). The surface of the birnessite seemed to peel off in many plate-like layers typical of phyllosilicate Mn oxyhydroxides [48]. These layers were partially wrapped, and in some places, it was possible to observe the interlayer of its structure (Figure 5b). Ranciéite were found to be elongated platelets (Figure 5c) from fractions of a few nanometers to micrometers in length (Figure 5d). The particles of ranciéite in all samples were found to be irregularly shaped platelets similar to those of birnessite under TEM (Figure 5). Under TEM, todorokite showed a strain-shaped morphology with parallel sides and regular termination, and occasionally, the longitudinal splitting of such fibers into thinner fibrils was observed (Figure 6). In some cases, todorokite fibers showed tight extremities assuming a conical morphology (Figure 6b). The fibrous todorokite was found in all samples, and always in conjunction with lamellar birnessite and/or ranciéite. It is worth remembering that todorokite fibers grow via the crack-and-seal mechanism [7]. Similar crack-and-seal structures are characteristic for the occurrences of chrysotile (asbestos) and asbestiform amphiboles in weakly metamorphosed formations [30–32]. Regarding the particle sizes detected using TEM, the todorokite fiber lengths in all samples ranged from a few nanometers to 10 µm, and from about 10 nm to 500 nm in width. In all the samples, most of the fibers measured were generally longer than 5 µm, with a width of < 3 µm and with aspect ratios > 3:1, and were therefore classified as asbestiform fibers [49,50].

The semi-quantitative chemical composition of several particles, as determined using TEM/EDS analyses, was in line with the general chemical composition of birnessite $(\text{Na,Ca})_{0.5}(\text{Mn})_2\text{O}_4 \cdot 1.5\text{H}_2\text{O}$, todorokite $(\text{Na,Ca,K,Ba,Sr})_{1-x}(\text{Mn,Mg,Al})_6\text{O}_{12} \cdot 3\text{-}4\text{H}_2\text{O}$, and ranciéite $(\text{Ca,Mn})_{0.2}(\text{Mn})\text{O}_2 \cdot 0.6\text{H}_2\text{O}$. The variation of the calcium percentage in the ranciéite and birnessite particles was used in order to discriminate between the two minerals, in agreement with Chukhrov et al. [51].

The chemical composition of the respective Mn oxyhydroxides hosted many major, minor, and trace elements. For example, todorokite had a variable composition where elements such as Zn, Mg, Ba, Sr, Ca, Na, K, Cu, Pb, and Ni could be detected in variable amounts. Calcium and alkali contents in birnessite fluctuated, and other elements, such as Mg, Ba, Zn, Cu, Co, Li, Al, and Fe, were also detected. These elements were often embedded in a sandwich-like manner as hydroxides in the form of disordered interlayers between well-ordered Mn oxyhydroxides or as Mn substitutes in the octahedral sites [45,48]. In ranciéite, variable amounts of Ca and Fe, and minor amounts of Mg, Al, Na, K, Si, P, and Cu were detected. As a matter of fact, variations in the chemical composition are linked with complex structure of Mn oxyhydroxides and can be explained easily by the manifold

substitutions of the cations [45]. In this regard, Mn oxyhydroxides' high reactive surface area particles play innumerable roles in the transformation and cycling of major and trace elements in hydrogenetic, diagenetic, and hydrothermal environments [52,53].

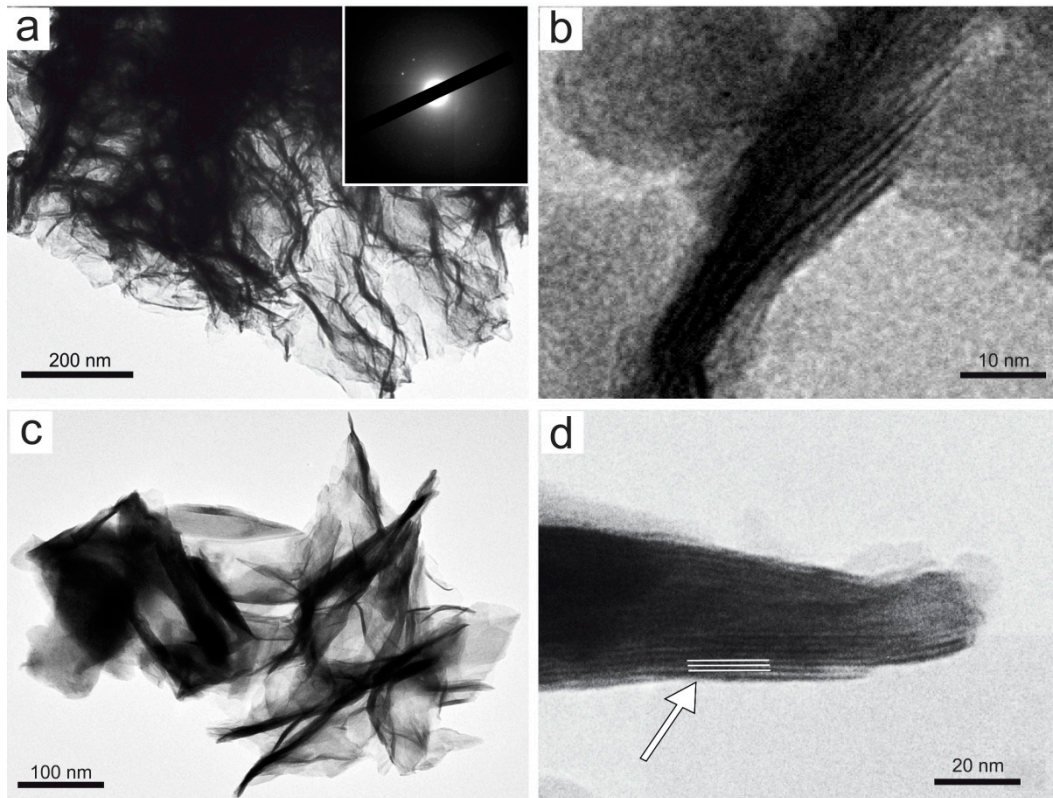


Figure 5. Representative TEM micrograph: (a) aggregates of sheet-like birnessite in sample 4S (the SAED pattern is shown in the inset); (b) detail of (a) where the interlayer of the birnessite structure is indicated by the black arrow; (c) rancièite occurrence as elongated platelets (sample 5S), and (d) detail of (c) where the interlayer spacing of rancièite structure of $\approx 8 \text{ \AA}$ is indicated by the white arrow.

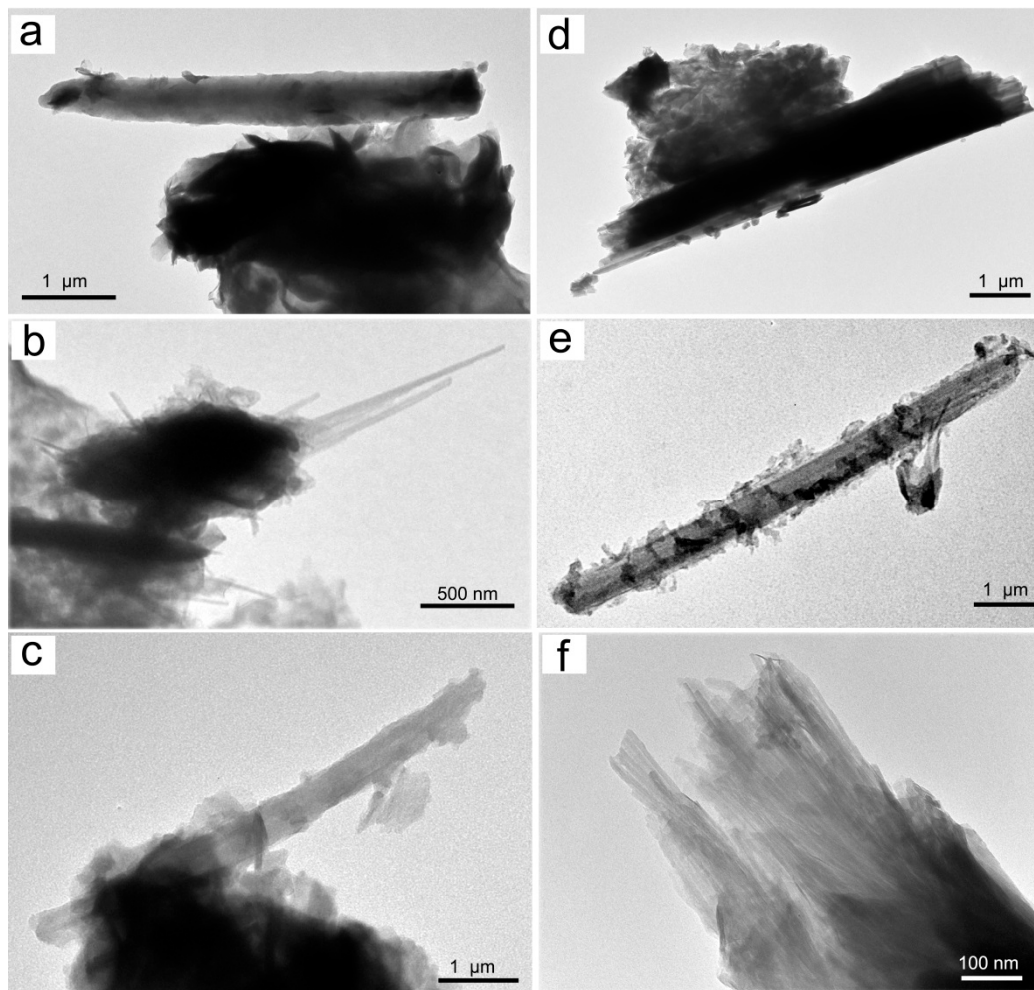


Figure 6. Representative TEM micrograph of the samples examined: (a) fibrous todorokite (sample 1S); (b) thin fibers of todorokite (sample 3S); (c) fibrous todorokite (note the curvature flexibility; sample 7S); (d) fibrous todorokite (cleavage fragment, note the irregular sides; sample 4S); (e) fibrous todorokite (sample 9S); and (f) bundle of todorokite fibers (sample 2S).

4.4. XRF Characterization

Through the X-ray fluorescence analytical technique, the following major and trace elements were found in the samples of manganese mineralization from Serra D’Aiello: MgO, Al₂O₃, SiO₂, P₂O₅, K₂O, CaO, TiO₂, MnO, Fe₂O₃, Na₂O, Rb, Sr, Cr, V, Ba, Ni, Co, Zn, Pb, and Cu. Tables 3 and 4 report the content of the oxides (in wt%) and trace elements (in ppm) for each sample.

As expected, MnO was the main component in all samples with mean values of 53.7 ± 8 wt% followed by SiO₂ and CaO (13 and 6 wt%, respectively).

The relatively high values of SiO₂, Al₂O₃, and K₂O were explained by the occurrence of minor amounts of silicate minerals, such as quartz, K-feldspar, plagioclase, and muscovite (Table 1).

Generally, a strong correlation did not exist between MnO and any other major elements (Table 3).

It is noteworthy to mention, however, that the mineralized beds contained some iron oxide abundances, which were separated by the manganiferous layers, suggesting that the solution from which the Mn precipitated also contained a fair amount of iron. It is good to note that in submarine hydrothermal Mn deposits, a common geochemical feature is the fractionation of Fe from Mn.

The initial precipitation of Fe-bearing phases is due to their higher precipitation rates with respect to Mn ones [54–58].

Concerning trace elements (Table 4), samples showed mutually comparable Sr, Cr, V, Zn, and Cu concentrations, whereas different distributions have been recognized for the remaining trace constituents (Ba, Ni, Co, and Pb). The high barium value in samples 5S and 9S was probably linked to the high content of rancéite detected, in which often the calcium present in its structure is replaced by barium [56]

In detail, samples 1S, 2S, 3S, 4S, and 5S showed anomalous Ni concentrations, close to or slightly below 500 ppm, which was different to what was highlighted in the remaining samples (below 150 ppm). Furthermore, samples 3S and 9S, and 4S and 6S, were characterized by high concentrations of Pb and Co, respectively (Table 3). High concentrations in these trace elements made them potentially available for subsequent accumulations in soils, water, and air with consequent negative effects on human health.

Table 3. Major element concentrations (in oxides wt%) obtained using XRF analysis. (LOI: loss on ignition). Fe₂O₃ stands for total Fe.

ID	LOI wt%	MgO wt%	Al ₂ O ₃ wt%	SiO ₂ wt%	P ₂ O ₅ wt%	K ₂ O wt%	CaO wt%	TiO ₂ wt%	MnO wt%	Fe ₂ O ₃ wt%	Na ₂ O wt%	Tot wt%
1S	14.21	3.50	5.33	15.32	0.34	1.13	9.20	0.34	47.58	2.72	0.32	100
2S	16.32	2.56	3.48	10.04	0.22	0.79	6.77	0.18	57.53	1.86	0.25	100
3S	15.57	3.34	3.19	9.62	0.09	0.46	4.17	0.13	61.76	1.53	0.13	100
4S	17.02	3.54	3.90	10.88	0.14	0.66	8.07	0.20	53.34	2.03	0.21	100
5S	16.09	2.18	2.44	7.52	0.14	0.45	4.10	0.25	65.38	1.44	0.15	100
6S	14.52	2.16	3.50	11.24	0.21	0.95	7.04	0.11	57.65	2.32	0.31	100
7S	14.59	2.52	4.55	13.27	0.27	0.81	7.46	0.20	53.64	2.27	0.40	100
8S	19.70	4.09	4.85	15.34	0.19	0.91	6.34	0.22	45.67	2.37	0.30	100
9S	13.83	6.40	6.69	23.24	0.12	1.06	4.29	0.28	40.92	2.87	0.30	100

Table 4. Trace element concentrations (in ppm) obtained using XRF analysis.

ID	Sr ppm	Cr ppm	V ppm	Ba ppm	Ni ppm	Co ppm	Zn ppm	Pb ppm	Cu ppm
1S	159	23	58	135	555	115	0	172	57
2S	153	14	28	114	511	38	0	75	57
3S	157	24	52	158	472	32	0	309	49
4S	160	24	27	132	509	566	0	169	65
5S	261	21	43	578	379	101	0	101	38
6S	254	11	22	112	94	298	37	92	56
7S	241	25	40	164	57	57	0	95	38
8S	219	24	55	125	151	94	0	0	57
9S	243	39	90	1086	127	109	54	746	73

Indeed, nickel compounds can cause a variety of adverse effects on human health, such as a nickel allergy in the form of contact dermatitis, lung fibrosis, cardiovascular and kidney diseases, and cancer of the respiratory tract [59–61]. In the same way, an excessive amount of cobalt exposure could cause a complex clinical syndrome with a varying set of neurological, cardiovascular, and endocrine deficits that are directly related to the uptake of Co ions in the tissue and in blood circulation [62]. Moreover, lead is also an extremely harmful environmental pollutant. If it is adsorbed, it can cause several negative affects to the respiratory and digestive body systems [63]. The threshold values of potential hazardous elements in each environmental matrix (soil, water, and air) are reported in Table S1 (Supplementary Materials). As such, defining the concentration of these compounds (minerals, elements) in these geological settings is the first step to limiting the exposure and consequently the problems that they can cause to those who live within the surrounding areas.

4.5. Origin of the Mn-rich Mineralizing Fluid

The geochemical characterization is an indispensable tool for understanding the genesis of Mn deposits. Using geochemical parameters, marine Mn deposits can be classified into three main types [1]:

(i) hydrothermal, (ii) hydrogenetic, and (iii) diagenetic deposits, as well as through a combination of these processes [57].

A $(\text{Cu} + \text{Ni} + \text{Co}) \times 10 - \text{Fe} - \text{Mn}$ diagram is usually used to identify the possible origin of Mn ores [64,65]. Figure 7 shows that the studied samples fell within the hydrothermal field. The high Mn/Fe ratio recorded suggests a typical deposit of a distal environment [9,66], which was also reflected by the lack of Fe phases in the selected Mn deposits.

Geochemical features of marine siliceous sediments, in particular the abundances of quartz and/or of its polymorphs common in deep-ocean floor sediments and in ophiolite sequences [67,68], have been studied to obtain information about their sources and depositional environments [69,70].

In response to this, the $\text{Al}/(\text{Al} + \text{Fe} + \text{Mn})$ and MnO/TiO_2 ratios were used to evaluate the relative contributions of the terrigenous and hydrothermal input of marine sediments, with Al and Ti being representative of a terrigenous source and Mn and Fe of a hydrothermal one, as reported by Kato et al. [71]. For the Serra D’Aiello samples, very low $\text{Al}/(\text{Al} + \text{Fe} + \text{Mn})$ values (lower than 0.04) and very high MnO/TiO_2 values (≈ 218) were detected. These ratios allowed us to exclude the option of a terrigenous input, suggesting that silica in the studied mineralizations may be indicative of further evidence of a hydrothermal origin (Figure 8).

Based on obtained data, and considering the geological setting of the studied area, this could suggest that hydrothermal processes have driven the deposition of the Mn-bearing minerals in the Serra D’Aiello sedimentary basin. The obtained results agree with those shown by Sinisi et al. [9], who have studied Mn-rich mineralization in the metasedimentary succession from the Calabria region (Italy).

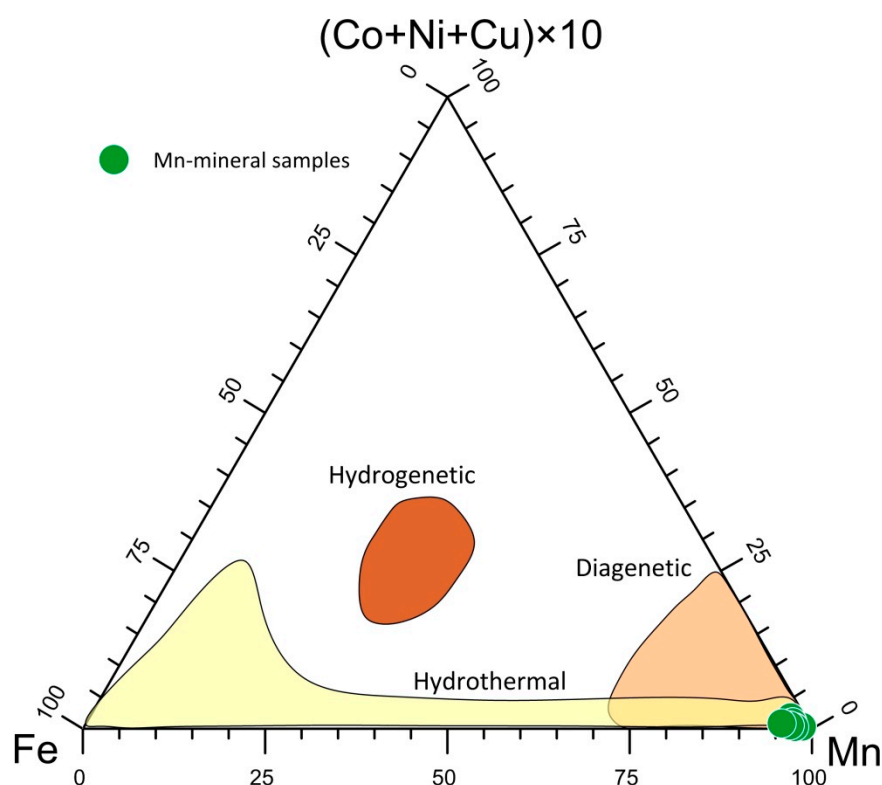


Figure 7. Triangular plot for the genesis discrimination of the Mn deposits.

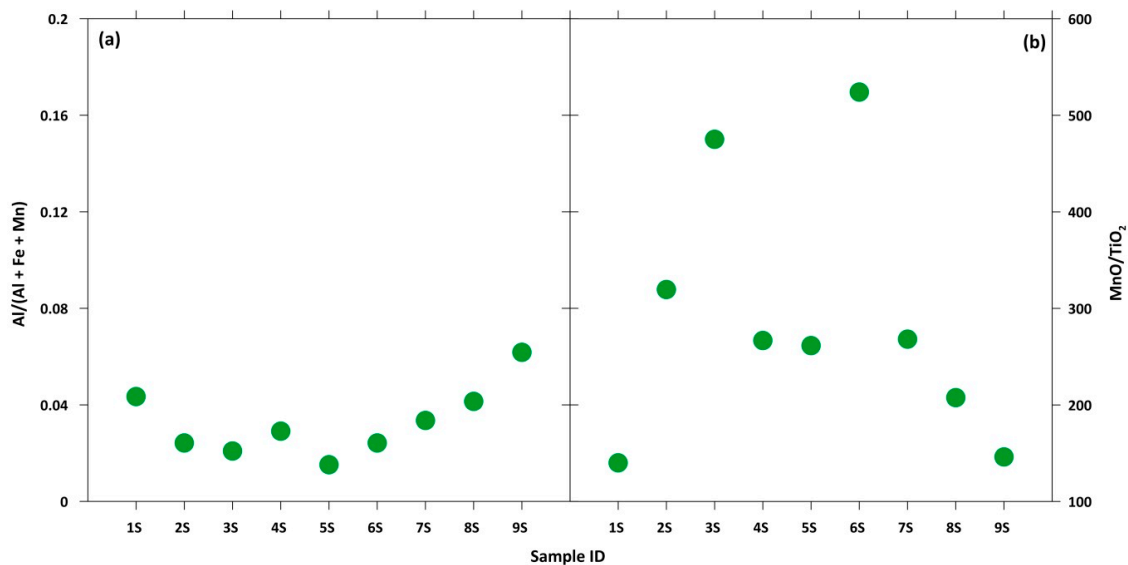


Figure 8. (a) Al/(Al + Fe + Mn) and (b) MnO/TiO₂ ratios for each sample.

5. Conclusions

A multidisciplinary approach based on mineralogical and geochemical analyses was used in order to characterize the Mn deposits from Serra D’Aiello (Southern Italy). The results obtained using XRPD, DSC/TG, TEM/EDS, and XRF showed that birnessite, todorokite, and ranciéite occurred as Mn oxyhydroxides phases in the analyzed samples. The Mn oxyhydroxides were poorly crystallized, and their morphology could only be recognized under TEM/EDS.

The release of Mn in the groundwater/soils, as well as other heavy metals from the Mn oxyhydroxide deposit, was regulated by a multitude of variables; therefore, the mineralogical and geochemical characterization of Mn oxyhydroxides minerals is important in order to define the potential environmental contamination in soils and groundwaters in areas where Mn oxyhydroxides occur. This investigation highlighted that ranciéite and birnessite with platy morphology occurred in all the analyzed samples, whereas the asbestiform todorokite was detected in seven samples.

Todorokite occurred in large amounts as microcrystalline fibrous–asbestiform phases in diagenetic rocks with fibers of breathable sizes (particles with length $\geq 5 \mu\text{m}$, width $\leq 3 \mu\text{m}$, length/width ratio $\geq 3:1$). It is important to note that, in addition to the minerals regulated as asbestos by law, asbestiform minerals, such as fibrous todorokite, could also potentially be dangerous if inhaled.

In the Amantea basin, a complete separation between Fe and Mn geochemistry during deposition and subsequent alteration was observed. This could be explained by an early segregation, with a release of a much greater abundance of Mn in comparison to Fe. From a geochemical point of view, some samples showed anomalous concentrations of Ni, Co, and Pb. The accumulations of these compounds in soils, water, and air can cause negative effects on human health, causing mild pathologies. Consequently, the widespread nature of both trace metals and asbestiform todorokite into the environment may be a cause of serious health problems for people who live near the sampling sites. For these reasons, an environmental monitoring plan in these potential contaminated sites is needed.

Finally, based on mineralogical and geochemical data, as well as considering the geological setting of the studied area, it was ascertained that hydrothermal processes have driven the Mn-bearing mineral deposition in the Serra D’Aiello sedimentary basin according to similar evidence presented in other metasedimentary successions outcropping in the Calabria region (Italy).

Supplementary Materials: The following are available online at <http://www.mdpi.com/2079-6439/8/2/9/s1>, Figure S1: XRPD pattern of the samples examined. Peaks were assigned according to the literature (International Centre for Diffraction Data (2005). ICDD Products/PDF-2, <http://www.icdd.com/products/pdf2.htm>). Table S1:

Threshold values of potential hazardous elements in soils and groundwaters (Italian Legislative Decree N°.152 of 03/04/2006) and air (NIOSH 2007).

Author Contributions: Conceptualization: A.B. and E.B.; methodology: A.B., G.V. and E.B.; formal analysis: A.B., G.V., I.F. and C.A.; investigation: A.B. and G.V.; data curation: A.B., G.V., I.F., E.B. and C.A.; writing—original draft preparation: A.B. and G.V.; writing—review and editing: A.B., D.M., R.D.R., G.V., I.F., R.D.L., E.B. and C.A.; visualization: A.B., G.V. and I.F.; supervision: A.B.; funding acquisition: A.B., D.M., R.D.R., R.D.L. and C.A. All authors have read and agreed to the published version of the manuscript.

Funding: This research received no external funding.

Acknowledgments: The authors thank M. Catalano for the support during data collection. The authors are also grateful to two anonymous reviewers for constructive comments and notes.

Conflicts of Interest: The authors declare no conflict of interest.

References

1. Hein, J.R.; Koschinsky, A.; Halbach, P.; Manheim, F.T.; Bau, M.; Kang, J.K. Iron and manganese oxide mineralization in the Pacific. In *Manganese Mineralization: Geochemistry and Mineralogy of Terrestrial and Marine Deposits*; Nicholson, K., Hein, J.R., Bühn, B., Dasgupta, S., Eds.; Geological Society Special Publication: London, UK, 1997; Volume 119, pp. 123–138.
2. Glasby, G.P. The mineralogy of manganese nodules from a range of marine environments. *Mar. Geol.* **1972**, *13*, 57–72. [[CrossRef](#)]
3. Belzile, N.; De Vitre, R.R.; Tessier, A. In situ collection of diagenetic iron and manganese oxyhydroxides from natural sediments. *Nature* **1989**, *340*, 376. [[CrossRef](#)]
4. Calvert, S.E.; Pedersen, T.F. Sedimentary geochemistry of manganese; implications for the environment of formation of manganiferous black shales. *Econ. Geol.* **1996**, *91*, 36–47. [[CrossRef](#)]
5. Muscente, A.D.; Czaja, A.D.; Tuggle, J.; Winkler, C.; Xiao, S. Manganese Oxides Resembling Microbial Fabrics and Their Implications for Recognizing Inorganically Preserved Microfossils. *Astrobiology* **2018**, *18*, 249–258. [[CrossRef](#)] [[PubMed](#)]
6. Vafeas, N.A.; Viljoen, K.S.; Blignaut, L.C. Characterization of Fibrous Cryptomelane from the Todorokite-cryptomelane Mineral Assemblage at the Sebilo Mine, Northern Cape Province, South Africa. *Can. Mineral.* **2018**, *56*, 65–76. [[CrossRef](#)]
7. Gutzmer, J.; Beukes, N.J. Asbestiform manjiroite and todorokite from the Kalahari manganese field, South Africa. *S. Afr. J. Geol.* **2000**, *103*, 163–174. [[CrossRef](#)]
8. Stoffers, P.; Glasby, G.P.; Frenzel, G. Comparison of the characteristics of manganese micronodules from the equatorial and south-west Pacific. *Tschermaks mineralogische und petrographische Mitteilungen* **1984**, *33*, 1–23. [[CrossRef](#)]
9. Sinisi, R.; Mongelli, G.; Perri, F.; Rizzo, G. The braunite (3Mn₂O₃·MnSiO₃)-rich mineralization in the metasedimentary succession from southern Apennines (Italy): Genesis constraints. *Ore Geol. Rev.* **2018**, *94*, 1–11. [[CrossRef](#)]
10. Glasby, G.P. Manganese: Predominant role of nodules and crusts. In *Marine Geochemistry*; Schulz, H.D., Zabel, M., Eds.; Springer: Berlin/Heidelberg, Germany, 2006; pp. 371–427.
11. Feng, X.H.; Zhu, M.; Ginder-Vogel, M.; Ni, C.; Parikh, S.J.; Sparks, D.L. Formation of nano-crystalline todorokite from biogenic Mn oxides. *Geochim. Cosmochim.* **2010**, *Ac. 74*, 3232–3245. [[CrossRef](#)]
12. Arias, N.P.; Becerra, M.E.; Giraldo, O. Structural and Electrical Studies for Birnessite-Type Materials Synthesized by Solid-State Reactions. *Nanomaterials* **2019**, *9*, 1156. [[CrossRef](#)]
13. Ertl, A.; Pertlik, F.; Prem, M.; Post, J.E.; Kim, S.J.; Brandstatter, F.; Schuster, R. Ranciéite crystals from Friesach, Carinthia, Austria. *Eur. J. Mineral.* **2005**, *17*, 163–172. [[CrossRef](#)]
14. Neculita, C.M.; Rosa, E. A review of the implications and challenges of manganese removal from mine drainage. *Chemosphere* **2018**, *214*, 491–510. [[CrossRef](#)] [[PubMed](#)]
15. Hernández-Pellón, A.; Fernández-Olmo, I. Using multi-site data to apportion PM-bound metal (loid) s: Impact of a manganese alloy plant in an urban area. *Sci. Total Environ.* **2019**, *651*, 1476–1488. [[CrossRef](#)] [[PubMed](#)]
16. Myeong, S.; Lee, K.H.; Kim, K.H. Airborne manganese concentrations on the Korean peninsula from 1991 to 2006. *J. Environ. Manag.* **2009**, *91*, 336–343. [[CrossRef](#)] [[PubMed](#)]

17. Riojas-Rodríguez, H.; Solís-Vivanco, R.; Schilman, A.; Montes, S.; Rodríguez, S.; Ríos, C. Intellectual function in Mexican children environmentally exposed to manganese living in a mining area. *Environ. Health Perspect.* **2010**, *118*, 1465–1470. [[CrossRef](#)] [[PubMed](#)]
18. Zoni, S.; Albini, E.; Lucchini, R. Neuropsychological testing for the assessment of manganese neurotoxicity: A review and a proposal. *Am. J. Ind. Med.* **2007**, *50*, 812–830. [[CrossRef](#)]
19. Bouchard, M.; Laforest, F.; Vandelac, L.; Bellinger, D.; Mergler, D. Hair manganese and hyperactive behaviors: Pilot study of school-age children exposed through tap water. *Environ. Health Perspect.* **2007**, *115*, 122–127. [[CrossRef](#)]
20. Kondakis, X.G.; Makris, N.; Leotsinidis, M.; Prinou, M.; Papapetropoulos, T. Possible health effects of high manganese concentration in drinking water. *Arch. Environ. Health* **1989**, *44*, 175–178. [[CrossRef](#)]
21. He, P.; Liu, D.H.; Zhang, G.Q. Effects of high-level-manganese sewage irrigation on children's neurobehavior. *Zhonghua Yu Fang Yi Xue Za Zhi* **1994**, *28*, 216–218.
22. Wasserman, G.A.; Liu, X.; Parvez, F.; Ahsan, H.; Levy, D.; Factor-Litvak, P.; Kline, J.; van Geen, A.; Slavkovich, V.; Llocacono, N.J.; et al. Water manganese exposure and children's intellectual function in Araihazar, Bangladesh. *Environ. Health Perspect.* **2006**, *114*, 124–129. [[CrossRef](#)]
23. Baumann, F.; Ambrosi, J.-P.; Carbone, M. Asbestos is not just asbestos: An unrecognised health hazard. *Lancet. Oncol.* **2013**, *14*, 576–578. [[CrossRef](#)]
24. Carbone, M.; Baris, Y.I.; Bertino, P.; Brass, B.; Comertpay, S.; Dogan, A.U.; Gaudino, G.; Jube, S.; Kanodia, S.; Partridge, C.R.; et al. Erionite exposure in North Dakota and Turkish villages with mesothelioma. *Proc. Natl. Acad. Sci. USA* **2011**, *108*, 13618–13623. [[CrossRef](#)] [[PubMed](#)]
25. Ballirano, P.; Bloise, A.; Gualtieri, A.F.; Lezzerini, M.; Pacella, A.; Perchiazzi, N.; Dogan, M.; Dogan, A.U. The Crystal Structure of Mineral Fibers. In *Mineral Fibers: Crystal Chemistry, Chemical-Physical Properties, Biological Interaction and Toxicity*; Gualtieri, A.F., Ed.; European Mineralogical Union: London, UK, 2017; Volume 18, pp. 17–53.
26. Gualtieri, A.F.; Gandolfi, N.B.; Passaglia, E.; Pollastri, S.; Mattioli, M.; Giordani, M.; Ottaviani, M.F.; Cangiotti, M.; Bloise, A.; Barca, D.; et al. Is fibrous ferrierite a potential health hazard? Characterization and comparison with fibrous erionite. *Am. Mineral. J. Earth Planet. Mater.* **2018**, *103*, 1044–1055. [[CrossRef](#)]
27. Petriglieri, J.R.; Laporte-Magoni, C.; Gunkel-Grillon, P.; Tribaudino, M.; Bersani, D.; Sala, O.; Salvioli-Mariani, E. Mineral fibres and environmental monitoring: A comparison of different analytical strategies in New Caledonia. *Geosci. Front.* **2020**, *11*, 189–202. [[CrossRef](#)]
28. NIOSH: National Institute for Occupational Safety and Health. *Asbestos Fibers and Other Elongate Mineral Particles: State of the Science and Roadmap for Research*; Current Intelligence Bulletin: Cincinnati, OH, USA, 2011; Volume 62.
29. Belluso, E.; Cavallo, A.; Halterman, D. Crystal habit of mineral fibres. In *Mineral Fibres: Crystal Chemistry, Chemical-Physical Properties, Biological Interaction and Toxicity*; Gualtieri, A.F., Ed.; Mineralogical Society of Great Britain and Ireland: Middlesex, UK, 2017; Volume 18, pp. 65–109.
30. Bloise, A.; Punturo, R.; Catalano, M.; Miriello, D.; Cirrincione, R. Naturally occurring asbestos (NOA) in rock and soil and relation with human activities: The monitoring example of selected sites in Calabria (southern Italy). *Ital. J. Geosci.* **2016**, *135*, 268–279. [[CrossRef](#)]
31. Bloise, A.; Barca, D.; Gualtieri, A.F.; Pollastri, S.; Belluso, E. Trace elements in hazardous mineral fibres. *Environ. Pollut.* **2016**, *216*, 314–323. [[CrossRef](#)]
32. Bloise, A.; Kusiorowski, R.; Lassinantti Gualtieri, M.; Gualtieri, A.F. Thermal behaviour of mineral fibers. In *Mineral Fibers: Crystal Chemistry, Chemical-Physical Properties, Biological Interaction and Toxicity*; Gualtieri, A.F., Ed.; European Mineralogical Union: London, UK, 2017; Volume 18, pp. 215–252.
33. Bloise, A.; Barrese, E.; Apollaro, C.; Fuoco, I.; Miriello, D.; Vespasiano, G. Todorokite, Ranciéite and Birnessite from Serra D'Aiello (Southern-Italy): New mineralogical and geochemical data. In Proceedings of the Congresso Società Geologica Italiana—Società di Mineralogia e Petrografia (SGI-SIMP) Catania, Sicily, Italy, 12–14 Settembre 2018.
34. Boni, M.; Rolandi, G. Mineralizzazioni manganesifere nel Messiniano del versante tirrenica della Catena Costiera Calabria (Serra d'Aiello). *Rend. Acc. Sc. Fis. Mat.* **1975**, *42*, 293–323.
35. Boni, M.; Rolandi, G.; Stanzione, D. Comportamento geochimico di alcuni elementi in tracce nelle mineralizzazioni manganesifere del Messiniano di Serra d'Aiello (Catena Costiera Calabria). *Ren. Acc. Sc. Fis. Mat.* **1976**, *42*, 492–509.

36. CASMEZ “Carta geologica della Calabria 1:25.000”, Poligrafica e Carte Valori; Central Calabria-Italy: Ercolano, Italy, 1967.
37. Cannata, C.B.; De Rosa, R.; Muto, F.; Davi, M. The pyroclastic level of Amantea Basin (Coastal Chain, north-western Calabria). *Rend. Soc. Geol. It.* **2012**, *21*, 887–888.
38. Muto, F.; Perri, E. Evoluzione tettono-sedimentaria del bacino di Amantea, Calabria occidentale. *Boll. Soc. Geol. It.* **2002**, *121*, 391–409.
39. Vespasiano, G.; Apollaro, C.; Muto, F.; De Rosa, R. Geochemical and hydrogeological characterization of the metamorphic-serpentinitic multiaquifer of the Scala catchment, Amantea (Calabria, South Italy). *Rend. Online Soc. Geol. It.* **2012**, *21*, 879–880.
40. Ortolani, F.; Torre, M.; Di Nocera, S. I depositi alto miocenici del bacino di Amantea (Catena Costiera Calabria). *Boll. Soc. Geol. It.* **1979**, *98*, 559–587.
41. Bloise, A.; Barrese, E.; Apollaro, C.; Miriello, D. Flux growth and characterization of Ti- and Ni-doped forsterite single crystals. *Cryst. Res. Technol.* **2009**, *2009* *44*, 463–468. [[CrossRef](#)]
42. Miriello, D.; Bloise, A.; Crisci, G.M.; Barrese, E.; Apollaro, C. Effects of milling: A possible factor influencing the durability of historical mortars. *Archaeometry* **2010**, *52*, 668–679. [[CrossRef](#)]
43. International Centre for Diffraction Data. ICDD Products/PDF-2. 2005. Available online: <http://www.icdd.com/products/pdf2.htm> (accessed on 8 December 2019).
44. Cheney, M.A.; Bhowmik, P.K.; Moriuchi, S.; Villalobos, M.; Qian, S.; Joo, S.W. The effect of stirring on the morphology of birnessite nanoparticles. *J. Nanomater.* **2008**, *10*, 1–9. [[CrossRef](#)]
45. Frenzel, G. The manganese ore minerals. In *Geology and Geochemistry of Manganese I*; Varentsov, I.M., Grasselly, G.Y., Eds.; Schweizerbart’sche Verlagsbuchhandlung: Stuttgart, Germany, 1980; pp. 25–157.
46. Straczek, J.A.; Horen, A.; Ross, M.; Warshaw, C.M. Studies of the manganese oxides. IV. Todorokite. *Am. Mineral. J. Earth Planet. Mater.* **1960**, *45*, 1174–1184.
47. Földvári, M. Handbook of thermogravimetric system of minerals and its use in geological practice. In *Occasional Papers of the Geological Institute of Hungary*; Geological Institute of Hungary: Budapest, Hungary, 2011; Volume 213.
48. Atkins, A.L.; Shaw, S.; Peacock, C.L. Nucleation and growth of todorokite from birnessite: Implications for trace-metal cycling in marine sediments. *Geochim. Cosmochim. Acta* **2014**, *144*, 109–125. [[CrossRef](#)]
49. World Health Organization (WHO). *Asbestos and Other Natural Mineral Fibres*; Environmental Health Criteria, 53; World Health Organization: Geneva, Switzerland, 1986.
50. Belluso, E.; Bellis, D.; Bruni, B.M.; Capella, S.; Coverlizza, S.; Ferraris, G.; Fornero, E.; Paoletti, E.; Rinaudo, C. Studio preliminare sulla valutazione indiretta delle fibre inorganiche respirabili aero disperse in Valle di Susa (Piemonte—Alpi Occidentali). *Rend. Soc. Geol. It.* **2007**, *3*, 41–45.
51. Chukhrov, F.V.; Gorshkov, A.I.; Rudnitskaya, E.S.; Beresovskaya, V.V.; Sivtsov, A.V. Manganese minerals in clays—A review. *Clays Clay Miner.* **1980**, *28*, 346. [[CrossRef](#)]
52. Toner, B.; Manceau, A.; Webb, S.M.; Sposito, G. Zinc sorption to biogenic hexagonal-birnessite particles within a hydrated bacterial biofilm. *Geochim. Cosmochim. Acta* **2006**, *70*, 27–43. [[CrossRef](#)]
53. Villalobos, M.; Bargar, J.R.; Sposito, G. Trace metal retention on biogenic manganese oxide nanoparticles. *Elements* **2005**, *1*, 223–226. [[CrossRef](#)]
54. Jach, R.; Dudek, T. Origin of a Toarcian manganese carbonate/silicate deposit from the Krízna unit, Tatra Mountains, Poland. *Chem. Geol.* **2005**, *224*, 136–152. [[CrossRef](#)]
55. Mcgregor, D.B.; Baan, R.A.; Partensky, C.; Rice, J.M.; Wilbourn, J.D. Evaluation of the carcinogenic risks to humans associated with surgical implants and other foreign bodies—A report of an IARC Monographs Programme Meeting. *Eur. J. Cancer* **2000**, *36*, 307–313. [[CrossRef](#)]
56. Barrese, E.; Gianpaolo, C.; Grubbessi, O.; Mottana, A. Rancieite from Mazzano Romano (Latium, Italy). *Mineral. Mag.* **1986**, *50*, 111–118. [[CrossRef](#)]
57. Bloise, A.; Ricchiuti, C.; Lanzafame, G.; Punturo, R. X-ray synchrotron microtomography: A new technique for characterizing chrysotile asbestos. *Sci. Total Environ.* **2020**, *703*, 135675. [[CrossRef](#)] [[PubMed](#)]
58. Critelli, T.; Vespasiano, G.; Apollaro, C.; Muto, F.; Marini, L.; De Rosa, R. Hydrogeochemical study of an ophiolitic aquifer: A case study of Lago (Southern Italy, Calabria). *Environ. Earth Sci.* **2015**, *74*, 533–543. [[CrossRef](#)]
59. Oller, A.R.; Costa, M.; Oberdörster, G. Carcinogenicity assessment of selected nickel compounds. *Toxicol. Appl. Pharmacol.* **1997**, *143*, 152–166. [[CrossRef](#)]

60. Seilkop, S.K.; Oller, A.R. Respiratory cancer risks associated with low-level nickel exposure: An integrated assessment based on animal, epidemiological, and mechanistic data. *Regul. Toxicol. Pharmacol.* **2003**, *37*, 173–190. [[CrossRef](#)]
61. Leyssens, L.; Vinck, B.; Van Der Straeten, C.; Wuyts, F.; Maes, L. Cobalt toxicity in humans—A review of the potential sources and systemic health effects. *Toxicology* **2017**, *387*, 43–56. [[CrossRef](#)]
62. Boskabady, M.; Marefati, N.; Farkhondeh, T.; Shakeri, F.; Farshbaf, A.; Boskabady, M.H. The effect of environmental lead exposure on human health and the contribution of inflammatory mechanisms, a review. *Environ. Int.* **2018**, *120*, 404–420. [[CrossRef](#)]
63. Bonatti, E.; Kraemer, T.; Rydell, H. Classification and genesis of submarine iron–manganese deposits. In *Papers from a Conference on Ferromanganese Deposits on the Ocean Floor*; Horn, D.R., Ed.; NSF: Alexandria, VA, USA, 1972; pp. 149–166.
64. Crerar, D.A.; Namson, J.; Chyi, M.S.; Williams, L.; Feigenson, M.D. Manganiferous cherts of the Franciscan Assemblage: I. General geology, ancient and modern analogues and implications for hydrothermal convection at oceanic spreading centers. *Econ. Geol.* **1982**, *77*, 519. [[CrossRef](#)]
65. Hein, J.R.; Bohrsen, W.A.; Schulz, M.S.; Noble, M.; Clague, D.A. Variations in the fine-scale composition of a central pacific ferromanganese crust: Paleoceanographic implications. *Paleocenography* **1992**, *7*, 63–77. [[CrossRef](#)]
66. Toth, J.R. Deposition of submarine crusts rich in manganese and iron. *Geol. Soc. Am. Bull.* **1980**, *91*, 44–54. [[CrossRef](#)]
67. Zarasvandi, A.; Rezaei, M.; Sadeghi, M.; Pourkaseb, H.; Sepahvand, M. Rare-earth element distribution and genesis of manganese ores associated with Tethyan ophiolites, Iran: A review. *Mineral. Mag.* **2016**, *80*, 127–142. [[CrossRef](#)]
68. Apollaro, C.; Fuoco, I.; Vespasiano, G.; De Rosa, R.; Cofone, F.; Miriello, D.; Bloise, A. Geochemical and mineralogical characterization of tremolite asbestos contained in the Gimigliano-Monte Reventino Unit (Calabria, south Italy). *J. Mediterr. Earth Sci.* **2018**, *10*, 5–15.
69. Apollaro, C.; Fuoco, I.; Brozzo, G.; De Rosa, R. Release and fate of Cr (VI) in the ophiolitic aquifers of Italy: The role of Fe (III) as a potential oxidant of Cr (III) supported by reaction path modelling. *Sci. Total Environ.* **2019**, *660*, 1459–1471. [[CrossRef](#)]
70. Murray, R.W.; Buchholtz Ten Brink, M.R.; Gerlach, D.C. Rare earth, major and trace elements in chert from the Franciscan Complex and Monterey Group, California: Assessing REE sources to fine grained marine sediments. *Geochim. Cosmochim. Acta* **1991**, *55*, 1875–1895. [[CrossRef](#)]
71. Kato, Y.; Nakao, K.; Isozaki, Y. Geochemistry of Late Permian to Early Triassic pelagic cherts from southwest Japan: Implications for an oceanic redox change. *Chem. Geol.* **2002**, *182*, 15–34. [[CrossRef](#)]



© 2020 by the authors. Licensee MDPI, Basel, Switzerland. This article is an open access article distributed under the terms and conditions of the Creative Commons Attribution (CC BY) license (<http://creativecommons.org/licenses/by/4.0/>).